Title

Conformational Dynamics of the HIV-Vif Protein Complex

Journal

Biophysical Journal, 116(8)

ISSN

0006-3495

Authors

Ball, K Aurelia

Chan, Lieza M

Stanley, David J

et al.

Publication Date

2019-04-01

DOI

10.1016/j.bpj.2019.03.014

Peer reviewed

Biophysical *Journal*
Article

Biophysical Society

Conformational Dynamics of the HIV-Vif Protein Complex

K. Aurelia Ball,[1,*] Lieza M. Chan,[1] David J. Stanley,[2] Elise Tierney,[1] Sampriti Thapa,[1] Hai M. Ta,[2] Lily Burton,[2] Jennifer M. Binning,[2] Matthew P. Jacobson,[2] and John D. Gross[2,*]
[1]Department of Chemistry, Skidmore College, Saratoga Springs, New York and [2]Department of Pharmaceutical Chemistry, University of California, San Francisco, San Francisco, California

ABSTRACT Human immunodeficiency virus-1 viral infectivity factor (Vif) is an intrinsically disordered protein responsible for the ubiquitination of the APOBEC3 (A3) antiviral proteins. Vif folds when it binds Cullin-RING E3 ligase 5 and the transcription cofactor CBF-β. A five-protein complex containing the substrate receptor (Vif, CBF-β, Elongin-B, Elongin-C (VCBC)) and Cullin5 (CUL5) has a published crystal structure, but dynamics of this VCBC-CUL5 complex have not been characterized. Here, we use molecular dynamics (MD) simulations and NMR to characterize the dynamics of the VCBC complex with and without CUL5 and an A3 protein bound. Our simulations show that the VCBC complex undergoes global dynamics involving twisting and clamshell opening of the complex, whereas VCBC-CUL5 maintains a more static conformation, similar to the crystal structure. This observation from MD is supported by methyl-transverse relaxation-optimized spectroscopy NMR data, which indicates that the VCBC complex without CUL5 is dynamic on the μs-ms timescale. Our NMR data also show that the VCBC complex is more conformationally restricted when bound to the antiviral APOBEC3F (one of the A3 proteins), consistent with our MD simulations. Vif contains a flexible linker region located at the hinge of the VCBC complex, which changes conformation in conjunction with the global dynamics of the complex. Like other substrate receptors, VCBC can exist alone or in complex with CUL5 and other proteins in cells. Accordingly, the VCBC complex could be a good target for therapeutics that would inhibit full assembly of the ubiquitination complex by stabilizing an alternate VCBC conformation.

INTRODUCTION

Human restriction factors provide a critical line of defense against viral pathogens. However, many viruses encode proteins to counteract restriction factors and allow for persistent infection in the host. A prime example of this host-pathogen conflict is provided by the human immunodeficiency virus (HIV)-1 protein viral infectivity factor (Vif), which targets the host antiviral APOBEC3 (A3) proteins. In the absence of Vif, A3 family members are encapsidated into HIV virions and inhibit viral replication primarily by deamination of cytidines to uridines in the viral complementary DNA during reverse transcription (1). The resulting hypermutation renders the viral infection nonproductive (2). Nearly all lentiviruses encode a Vif protein that counteracts the A3 family members, targeting them for destruction by ubiquitin-mediated proteolysis (3). Vif hijacks a Cullin-RING E3 ligase (CRL), which acts in the last step of a three-enzyme E1-E2-E3 ubiquitination cascade. HIV-1 Vif recruits A3 family members to CRL5, which contains the adaptor proteins Elongin-B (ELOB) and Elongin-C (ELOC) as well as the scaffold protein, Cullin5 (CUL5), and a RING-box protein. As shown in Fig. 1 *b*, Vif hijacks CRL5 by replacing suppressor of cytokine signaling (SOCS)2 (Fig. 1 *a*) as the substrate-binding protein, interacting directly with ELOC and CUL5 (4). Vif also recruits core-binding factor subunit-β (CBF-β), a transcription cofactor, to the CRL5 complex (5,6). Although not present in the cellular E3 ligase complex, CBF-β is required for the formation of a functional HIV-1 Vif E3 holoenzyme both in vitro and during HIV infection (5,6).

Vif is an intrinsically disordered protein (7), yet Guo et al. (4) solved a crystal structure of a complex between Vif, CBF-β, ELOB, ELOC, (termed VCBC) and the N-terminal domain of CUL5 (CUL5ntd). This structure revealed that the four-protein VCBC is a cofolded unit and that Vif is folded into a larger α/β-domain (residues 1–111, 166–176) and a smaller α-domain (residues 116–126, 145–153) that are connected through a linker region (residues 112–115, 127–144, 154–165) containing a zinc-binding motif (4), as shown in Fig. 1 *d*. For this A3 substrate receptor

Submitted November 29, 2018, and accepted for publication March 2, 2019.
*Correspondence: kball@skidmore.edu or jdgross@cgl.ucsf.edu
Editor: Monika Fuxreiter.
https://doi.org/10.1016/j.bpj.2019.03.014

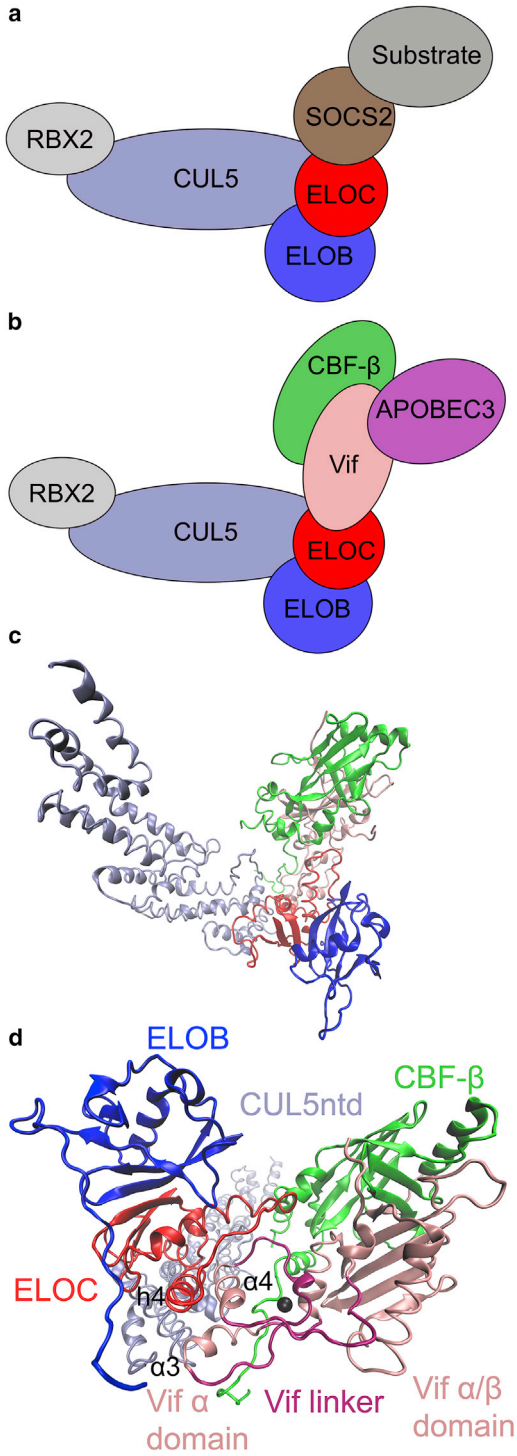

FIGURE 1 Schematic diagram of (*a*) the host SOCS-CLR5 E3 ubiquitin ligase complex and (*b*) the HIV-Vif E3 ubiquitin ligase complex. The VCBC-CUL5ntd crystal structure (PDB: 4N9F) is shown from the same orientation as the diagram (*c*) and rotated (*d*) to more clearly show the two Vif domains connected by the Vif linker region (residues 112–115, 127–144, 154–165) in dark pink containing the zinc ion shown as a black sphere. Vif helices α3 and α4 and ELOC helix h4 are labeled. To see this figure in color, go online.

complex to form, Vif must adopt a folded conformation, stabilized by interactions with CBF-β and the ELOB and ELOC heterodimer (ELOBC) (6). The α-domain of Vif binds ELOBC and CUL5 by mimicking the SOCS2 interaction surface. It contains a BC-box motif required to interact with ELOBC and a surface that directly binds CUL5 (Fig. 1 *d*). The α/β-domain of Vif is responsible for interacting with CBF-β, and through this interaction, CBF-β stabilizes the two loosely packed helices in the α/β-domain of Vif and forms an extended intermolecular β-sheet with the N-terminus of Vif (4–6). Between these two domains, whose secondary structure is stabilized by their interacting partners, the Vif linker region is less structured, stabilized by a zinc ion that interacts with the HCCH arrangement of His and Cys residues in the Vif linker region (4). We hypothesized that this unstructured linker region, located in the center point of the VCBC structure, may form a hinge that determines flexibility and conformational changes of the complex. Although the intrinsically disordered Vif protein folds as part of the CRL complex, flexibility retained in the linker region may be critical to allowing different regions of the complex to reorient, allowing ubiquitination of the A3 protein to occur.

CUL5ntd is present in the Guo et al. (4) crystal structure, but it is not required for Vif to form the stable VCBC complex (6). Rather, CUL5 stabilizes the already formed VCBC complex when it binds (4). The Vif HCCH zinc-binding motif is required for CUL5 binding, although it does not directly interact with CUL5 (4). As noted by Guo and Zhou (8), sometimes when a protein partner (like CUL5) is removed, favorable interactions are lost, causing proteins to sample more states and show an increase in conformational entropy. Furthermore, a multitude of substrate receptors must share a given CRL backbone, which is promoted by cycles of NEDD8 conjugation, deconjugation, and substrate receptor exchange (9). There are also at least three distinct A3 protein-binding interfaces on Vif: the APOBEC3F-like binding site, which binds APOBEC3F, APOBEC3C, and APOBEC3D; the APOBEC3G-binding site; and the APOBEC3H-binding site (10,11). Each A3 protein may also have different binding affinities for different conformations of the VCBC complex. Accordingly, understanding the structural dynamics of the VCBC subunit not bound to the CUL5 scaffold could be advantageous for understanding the complete process of A3 ubiquitination by Vif. Additionally, full assembly of the CRL complex potentially could be inhibited if alternate conformations of the VCBC complex incompatible with CUL5 binding are stabilized, for example, by small-molecule binding.

Previous molecular dynamics (MD) simulation studies by Liu and Nussinov (12–14) have shown that ubiquitination complexes are flexible. In their simulations of several CRL complexes (CUL1 and CUL5 complexes), they found that conformations different from those in the crystal structure

are sampled. Specifically, the substrate-binding protein that links the adaptor (ELOBC in our case) to the substrate (an A3 protein in our case) was found to contain a flexible linker region that allowed the substrate-binding domain to reorient relative to the BC-box domain (12,13). Liu and Nussinov (12,13) also found that this conformational flexibility was allosterically regulated by binding of both the adaptor and substrate proteins, sometimes restricting the conformations sampled. In the VCBC complex, Vif plays the role of the substrate-binding protein, with the help of CBF-β, and also contains a linker region between its two domains. No structures have been solved with Vif bound to an A3 protein, but several mutational studies have been performed that indicate the interfaces on the α/β domain of Vif where the A3s bind (15,16). Because the Vif-ubiquitination complex performs the large-scale transfer of the ubiquitin moiety from the E2 at one end of the complex to the substrate at the other, alternate conformations could be important for function of the complex (12). In this study, we compare the conformational ensembles and alternate states of the HIV-1 Vif complex and investigate the role Vif plays in the flexibility of the complex.

We used MD simulations and NMR spectroscopy to investigate conformational dynamics of the Vif substrate receptor complex. Simulations enable direct comparison of conformational states for the VCBC complex with and without CUL5ntd bound, including states that may be difficult to capture experimentally because of their low occupancy. We found that the VCBC-CUL5ntd complex samples conformations similar to the crystal structure, whereas the VCBC complex undergoes large-scale conformational changes involving the flexible linker region of Vif. MD simulations of VCBC bound to APOBEC3F (A3F) based on a modeled interface (17) also indicated that the VCBC complex is conformationally restricted when bound to the C-terminal domain of A3F (A3Fctd). We also carried out methyl-transverse relaxation-optimized spectroscopy (methyl-TROSY) NMR experiments, which support the existence of multiple alternate conformations of the VCBC complex that interconvert on the μs-ms timescale, causing extensive peak broadening; however, the VCBC complex bound to A3Fctd (VCBC-A3Fctd) displays reduced VCBC dynamics. Thus, both computational simulations and NMR experiments demonstrate that the HIV-1 Vif substrate receptor (VCBC) is a dynamic complex that samples multiple conformations, and these dynamics are partially quenched upon binding to substrate or additional E3 ligase components. Structural adaptability in Vif is likely important for it to bind multiple A3 proteins through different binding modes and to carry out the catalytic step of ubiquitin transfer. By revealing alternate conformational states, simulations could also provide strategies to discover future therapeutics that inhibit A3 ubiquitination and degradation, resulting in A3 encapsidation and inhibition of viral replication.

MATERIALS AND METHODS

Model building and system preparation

Crystal structures are available for VCBC-CUL5ntd (Fig. 1) and A3Fctd. MD simulations were run on four different constructs of the HIV-Vif complex: VCBC, VCBC-CUL5ntd, VCBC-A3Fctd, and VCBC with the shorter ELOB102. The initial coordinates for each of these simulations came from the crystal structure of VCBC-CUL5ntd (Protein Data Bank (PDB): 4N9F) (4). The crystal structure PDB file was missing coordinates for several unstructured regions of the proteins: Vif 1–2 and 173–176, CBF-β 1 and 157–165, ELOB 80–82 and 99–102, ELOC 50–57 and 112, and CUL5 119–130. These were built using the PLOP homology modeling software to predict the conformation of the missing residues (18). Because the HIV-Vif consensus sequence was used for the NMR experiments (19), a homology model of the consensus Vif was built in Prime (20,21). Histidine protonation states were optimized using Maestro (22). The crystal structure of VCBC-CUL5ntd contained a truncated ELOB protein of only 102 residues, whereas the wild-type ELOB has 118 residues. Therefore, for all simulated constructs except VCBC with ELOB102, the starting structure for the C-terminus of ELOB was obtained from a crystal structure of the HIV-Vif SOCS-box of ELOBC (PDB: 2MA9), which has the full-length ELOB (23). To combine the two structures, residues 1–78 of ELOB were aligned in the two structures using visual MD (VMD) (24,25), and residues 79–102 of ELOB from 4N9F were replaced with residues 79–118 of ELOB from 2MA9. For the VCBC and VCBC-A3Fctd constructs, the CUL5ntd atoms were removed.

For the simulations of VCBC-A3Fctd, the starting structure was obtained from the model by Richards et al. (17) provided as a PDB file in the Supporting Materials and Methods. To combine the Guo et al. (4) VCBC-CUL5ntd crystal structure with the Richards et al. (17) modeled structure of the A3F-Vif interface, the Vif interface residues (42–52 and 75–85) were aligned in the two structures using VMD (24), and the structure of A3Fctd from the Richards et al. (17) model was added to the VCBC structure. Because the solubility-enhanced A3Fctd construct used in our NMR experiments had 11 mutations (Y196D, H247G, C248R, C259A, F302K, W310D, Y314A, Q315A, K355D, K358D, F363D), our simulations were performed on this construct for comparative purposes. The VCBC-A3Fctd structure was changed to match this experimental sequence, and the mutated side chains were modeled in with LEaP (26). Six missing residues at the N-terminus of the A3Fctd were modeled in using PLOP (21).

The Amber99SB protein force field was used for our MD simulations with the TIP3P water model (27,28). The Amber 16 LEaP module was used to prepare each complex for simulation and create Amber parameter and input coordinate files. To model zinc ions and coordinated residues, we treated the zinc ion with a four-point charge representation as reported (29). The proteins were surrounded with at least 10 Å of water on all sides in a periodic box, and Na^+ ions were added to neutralize the system (Table S1).

MD simulations

Energy minimization was performed for each complex before running MD simulations, initially with restraints of 500 kcal/(mol-Å^2) on the protein atoms to allow the solvent to minimize and then with no restraints to allow the protein structure to minimize away from any high-energy residue conformations. 500 steps of steepest descent minimization were performed followed by 1000 steps of gradient minimization for each round. The systems were then equilibrated for 20 ps at constant volume while raising the temperature from 0 to 300 K, with restraints of 10 kcal/(mol-Å^2) on protein atoms. Two more constant-pressure equilibrations were performed to equilibrate the density of the systems with 1 kcal/(mol-Å^2) restraints on the protein for 20 ps and then without restrains for 1 ns. Dimensions of the periodic box after equilibration for each construct are given in Table S1. All MD simulations were performed on GPUs using the CUDA

version of the *pmemd* module in the Amber package (26). The Andersen thermostat was used to hold the temperature constant at 300 K (30,31), and the Berendsen barostat with isotropic position scaling and a relaxation time of 1 ps was used to hold the system at 1 bar (32). The particle mesh Ewald procedure was used to handle long-range electrostatic interactions with a nonbonded cutoff of 9 Å. After the initial 1-ns equilibration, four or eight independent production simulations were run for each construct starting from the same equilibrated structure but with new initial, randomized velocities. For the VCBC and VCBC-CUL5ntd constructs, eight independent simulations were run, whereas only four independent simulations were run for the VCBC-A3Fctd and truncated ELOB VCBC constructs. The total simulation time for each construct is given in Table S1. Snapshots were saved every 5 ps for the production simulations. The first 100–300 ns of each simulation was treated as equilibration to allow the structure to relax away from the crystal structure. Only the last 300 ns of data from each simulation were analyzed.

Structure and trajectory analysis

Analysis of the MD simulations was performed using the *cpptraj* module of Amber (26) and in-house Python scripts. Interatomic distances, dihedral angles, root mean-square deviation (RMSD) of protein structures, root-mean-square fluctuations, and hydrogen-bond percentages were all calculated using *cpptraj*. Cartesian principal component analysis (PCA) was also calculated with *cpptraj*,based on the C_α position for each residue in the structured regions of the VCBC complex (excluding flexible tails and loops). The principal components (PCs) were taken as the first eigenvectors, v, of the covariance matrix, M, for these C_α positions. The data used to construct this covariance matrix included the ensemble of structures from both the VCBC simulations and the VCBC-CUL5ntd simulations. The data from each of the simulated constructs were then projected onto these same PCs to compare the global motions of the VCBC complex for each system.

To determine which distances between two residues correlated most with each PC, we divided the PC into three components (x, y, and z) that corresponded to each C_α atom and took the dot product between all combinations of C_α atom vectors. The two atoms that yielded the most negative dot product were moving the most in opposite directions as the system moves along that PC, indicating that those atoms are getting closer together or farther apart.

All histograms were computed by combining the independent simulations for a given construct (snapshots spaced every 50 ps) and binning over this total ensemble of structures. To determine the timescale of the VCBC conformational exchange, the autocorrelation time, τ, was calculated for each metric. Because the autocorrelation time for the first two PCs was only one order of magnitude smaller than our total simulation time for each independent simulation, we treated the data from one simulation as correlated for purposes of statistical analysis. Only data from separate simulations were treated independently. All protein structure figures were created using VMD (24,25). To cluster the VCBC ensemble by PCs 1 and 2, we used the agglomerative clustering method in the Python machine learning module, scikit-learn (33), which recursively merges pairs of clusters that minimally increase a given linkage distance. We used the Ward linkage, which minimizes the variance of the clusters being merged so that there will be greater variance in the data in different clusters than within one cluster. The number of clusters was set to three because we observed two very similar clusters when we increased the number to four clusters. To sort the VCBC-CUL5ntd data into clusters, we fit a linear support vector classification machine to the VCBC clusters with scikit-learn (33) and used that fit to predict the VCBC-CUL5ntd cluster membership. In this way, different regions of the PC1 versus PC2 plot were designated as belonging to each of the three different clusters.

To compare PC1 and PC2 for VCBC-CUL5ntd with each of the other constructs, we calculated the p-values for the mean and variance using a permutation test. The square of the difference between the mean of each independent simulation and the crystal structure, as well as the variance within each independent simulation were used to determine p-values. All p-values were found using 10,000 permutations.

To determine the mean dihedral angle in our ensembles, we converted the angles to radians and calculated the exponential,

$$e^{i\theta},$$

where i is the imaginary number $\sqrt{-1}$ and θ is the dihedral angle. We then summed this exponential over all the structures in our trajectory and found the angle of the complex argument for the sum, which is the average dihedral angle, accounting for periodicity. We similarly accounted for periodicity when calculating average differences in dihedral angles and dihedral RMSD.

Assessment of simulation convergence

To make sure that we compared simulations that had equilibrated sufficiently away from the initial crystal structure, we divided each of the simulations into 100-ns blocks and performed PCA on the ensemble of structures from four independent simulations for each block. Table S2 shows the first five eigenvalues for each block. We then took the sum of the first five eigenvalues, which corresponds to the variance captured by the first five PCs, and plotted how this quantity changes for each simulation block (Fig. S1). We observed that for the VCBC-CUL5ntd and VCBC simulations, the variance increased and then reached a value that was steady over multiple windows.

The σ-r plots for all constructs were made to show the average range of motion between α carbons as a function of interatomic distance for each 100-ns block of simulation (34). The average interatomic distances between α carbons were calculated for each pair of residues, along with the SD. The SDs within intervals of $\Delta r = 0.5$ Å were averaged to determine the average σ values for the interatomic distance interval using the equation

$$\sigma_r = \frac{1}{N}\sum \sigma_{i,j},$$

where N is the number of interatomic distances within the range

$$r - \frac{\Delta r}{2} < r_{i,j} \leq r + \frac{\Delta r}{2},$$

and $r_{i,j}, \sigma_{i,j}$ are the mean interatomic distance and SD of the distance between α carbons i and j over 100-ns blocks of the construct trajectories. The values calculated for each 100-ns block were graphed, and the SDs were calculated using the independent simulations.

Protein expression and purification

The VCBC complex, consisting of consensus Vif (19), CBF-β (residues 1–165), ELOB (residues 1–118), and ELOC (residues 17–112), was coexpressed in *Escherichia coli* BL21 DE3 Star cells as described (19). Briefly, cells were grown to midlog phase at 37°C followed by induction with isopropyl β-D-1-thiogalactopyranoside at 18°C for 18 h. Cells were harvested and subsequently lysed by sonication in nickel buffer A (20 mM HEPES (pH 8), 500 mM NaCl, 10% glycerol, 1 mM dithiothreitol [DTT], 20 mM imidazole), followed by centrifugation (14,500 × g, 45 min, 4°C) to clarify the lysate. The sample was purified by nickel chromatography, a heparin column, and size-exclusion chromatography (SEC) into a pH 7.5 buffer containing 20 mM HEPES, 500 mM NaCl, 10% glycerol, and 1 mM DTT. To form the VCBC-dT14 complex, purified VCBC was concentrated and combined with oligonucleotide DNA (dT14) in a 1.5:1 ratio of protein to oligonucleotide, then diluted with 20 mM HEPES (pH 7.5) to an NaCl concentration less than 40 mM, and purified by SEC in 20 mM

HEPES, pH 7.5 buffer with 0.5 mM tris(2-carboxyethyl)phosphine (TCEP) and 20 mM NaCl with no glycerol.

To express the VCBC complex with ^{13}C isotope labels on the methyl groups (Ile, Leu, Val, Met, and Ala (ILVMA)) for NMR spectroscopy, the BL21 DE3 Star cells were grown in M9 minimal media with trace metals (35). Before inducing with isopropyl β-D-1-thiogalactopyranoside, ^{13}C isotope-labeled amino acid precursors were added to the culture [50 mg/L 2-ketobutyric adid-4-^{13}C, 100 mg/L 2-keto-3 methyl-^{13}C-butyric acid-4-^{13}C, 250 mg/L *L*-Methionine-methyl-$^{13}C1$, 100 mg/L *L*-Alanine (3-^{13}C)].

A solubility-optimized form of the A3F-C-terminal domain with 11 mutations was expressed in *E. coli* BL21 DE3 Star cells as described (19,36). The sample was purified by nickel chromatography, and the His-tag was cleaved with the tobacco etch virus (TEV), then passed again over the nickel column to remove the tag. The A3Fctd sample was then further purified by SEC with a HiLoad Superdex 75 prep grade column purchased from GE Healthcare (Chicago, IL). Budding yeast Upf1 was expressed and purified as described (37).

Gel-shift assays

Poly(U)40 oligonucleotide (Dharmacon, Lafayette, CO) was end labeled by polynucleotide kinase with [γ-32P] ATP, according to the manufacturer's recommendations (New England Biolabs, Ipswich, MA). Reaction products were purified with an Illustra G-50 column (GE Healthcare). 100-pmol probe RNA was mixed with buffer or varying amounts of protein in NEBuffer 2 (New England Biolabs) and incubated at room temperature for 15 min. Native gel electrophoresis followed by phosphorimaging (Typhoon; GE Healthcare) was used to visualize the formation of RNA-protein complexes.

RNase protection

Body-labeled poly(U) RNA was synthesized by a tailing reaction with poly(U) polymerase (New England Biolabs), poly$(U)_{15}$ oligonucleotide primer, and [α-^{32}P] UTP. Long RNAs were purified using an RNeasy Mini Spin Column (QIAGEN, Hilden, Germany) according to the manufacturer's recommendations. For each RNase protection assay, 1 μL of 2×10^5 cpm/μL body-labeled poly(U) RNA was mixed with either 2 μM protein or buffer in 1/2$\times$ NEBuffer 2. RNase A was added at a final concentration of between 2 and 10 μg/mL, and reactions were mixed and allowed to proceed for 1 h at room temperature. Nuclease-resistant products were purified by two successive chloroform-phenol extractions followed by ethanol precipitation overnight at -80°C. Inclusion of glycogen at a final concentration of 15 μg/mL during ethanol precipitation was critical for the recovery of small RNA fragments. Finally, reaction products were visualized by denaturing gel electrophoresis and phosphorimaging (Typhoon; GE Healthcare) followed by analysis in ImageJ (38).

Fluorescence anisotropy

5′ fluorescein-labeled and unlabeled oligonucleotides were purchased from Integrated DNA Technologies (Coralville, IA). All measurements were made using an Analyst AD system (LJL BioSystems, Sunnyvale, CA). For direct binding assays, VCBC was serially diluted into a solution containing 25 mM HEPES (pH 7.9), 25 mM NaCl, 1.25 mM MgCl2, 1 mM DTT, and 1 nM fluorescent probe. For competitive binding assays, an unlabeled competitor oligonucleotide was diluted into a solution containing 25 mM HEPES (pH 7.9), 25 mM NaCl, 1.25 mM MgCl2, 1 mM DTT, 0.5 nM fluorescent probe, and VCBC at a concentration equal to the K_d value determined for probe-VCBC binding. All data were fit in R using the *minpack.lm* package (39); direct binding experiments were fit using a single-site saturation binding model, and competitive binding experiments were fit as described (40). Plots were generated using the ggplot2 package for R (41).

Methyl-TROSY NMR spectroscopy

NMR was performed in 20 mM HEPES (pH 7.5) D_2O buffer with 20 mM NaCl and 0.5 mM TCEP. NMR experiments were performed on an 800-MHz Bruker spectrometer (Billerica, MA) with a cryogenically cooled probe. Methyl-TROSY experiments were performed at 300 K (42). The VCBC concentration was $\sim$160 μM for the VCBC-dT14 experiment, and 256 scans were performed in the ^1H dimension, and 128 complex points were acquired in the indirect ^{13}C dimension. The A3Fctd concentration was $\sim$108 μM and the VCBC concentration was $\sim$90 μM for the VCBC-dT14-A3Fctd experiment, and to adjust for this concentration difference, 816 scans were performed in the ^1H dimension and 128 complex points were acquired in the indirect ^{13}C dimension. The relative differences in concentration of VCBC for the two experiments were well determined because the VCBC samples came from the same stock solution. Spectra were processed using the NMRPipe suite of programs (43). Figures and chemical shift assignments were done using the Python module nmrglue (44). Remaining data analysis was performed using in-house Python scripts.

Isothermal titration calorimetry

The binding affinity between A3Fctd and VCBC was measured using a VP-ITC Micro Calorimeter (MicroCal, Los Angeles, CA). The proteins A3F and VCBC were dialyzed extensively against either high-salt buffer (20 mM HEPES (pH 7.5), 10% glycerol, 300 mM NaCl (A3F into VCBC monomer)) or low-salt buffer (20 mM HEPES (pH 7.5), 10% glycerol, 50 mM NaCl, 2 mM dT14 (A3F into VCBC dimer)) before titration. The injection syringe and the sample cell were filled with A3F and VCBC, respectively. The system was equilibrated to a stable baseline before initiating an automated titration. Each titration experiment injected 7 μL of A3F, and 30 injections were repeated at 200-s intervals at 25°C. The sample cell was stirred at 300 rpm. Heat changes upon the addition of the A3F were monitored and fitted using the least-squares regression analysis of ORIGIN software (MicroCal, Los Angeles, CA) to calculate the dissociation constant (K_d).

SEC multiangle laser light scattering

To determine the molecular size of VCBC monomer and dimer, the purified proteins were injected into a Shodex KW-804 size-exclusion column with an Ettan LC (GE Healthcare), and the elution products were applied to in-line DAWN HELEOS multiangle light scattering and Optilab rEX differential refractive index detectors (Wyatt Technology, Santa Barbara, CA). Data were analyzed by the ASTRA V software package (Wyatt Technology).

RESULTS

Alternate conformations of the VCBC complex

Simulations of VCBC and VCBC-CUL5ntd

We performed MD simulations of the VCBC complex alone or bound to CUL5ntd. In both simulations we observed large-scale global motions of the complex and flexibility in the Vif linker region, near the Zn^{2+} coordination site. We used Cartesian coordinate PCA to identify the global motions that were most dominant in our simulations. To compare the VCBC and VCBC-CUL5ntd simulations, we performed PCA on the combined ensemble of all the

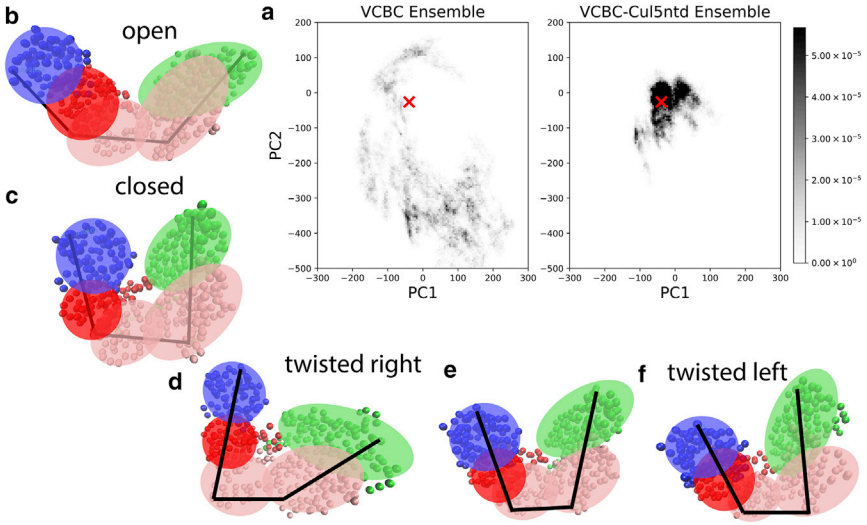

FIGURE 2 (*a*) Projection of the VCBC and VCBC-CUL5ntd ensembles onto the first two PCs of motion (Å). The shading of the cell represents the fraction of the ensemble at that value of PC1 and PC2, where black is 5.4×10^{-5} or greater and white is 0. The red x represents the values of PC1 and PC2 in the crystal structure from which all simulations were initiated. (*b* and *c*) PC2 represented as Cα positions in the range plotted, with a cartoon overlaid, is shown. Vif is shown in pink, CBF-β in green, ELOB in blue, and ELOC in red. (*d–f*) PC1 represented as a series of Cα positions in the range plotted, with a cartoon overlaid, is shown. To see this figure in color, go online.

VCBC structures from the last 300 ns from both the VCBC and VCBC-CUL5ntd simulations. The first two PCs accounted for ~71% of the variance in the VCBC structure over both sets of simulations (with and without CUL5ntd). The first PC (48% of the variance) involved a twisting open of the Vif α/β domain and CBF-β with respect to the Vif α-domain and ELOBC, whereas the second PC (23% of the variance) captured a clamshell motion where the Vif α/β domain and CBF-β come closer to ELOBC (Fig. 2). Fig. 2 shows that although the simulations with CUL5ntd do include a small amount of sampling along these PCs, the VCBC conformational ensemble in the absence of CUL5 is much more heterogeneous. VCBC samples conformations that are substantially different from the crystal structure both in PC1 and in PC2. This indicates that VCBC adopts alternate conformational states not present when CUL5ntd is bound. Table 1 shows the mean and SD for PC1 (twisting motion) and PC2 (clamshell motion) for each construct. The same types of motions are also occurring for VCBC-CUL5ntd (Fig. 2), but the total conformational change is not as large.

We measured the autocorrelation time for each of the first two PCs to determine the timescale of the motions that these PCs are capturing. VCBC exhibited autocorrelation times of ~25 ns for both PC1 and PC2, meaning that (at least) hundreds of nanoseconds of simulation time would be required to fully sample those motions. To make sure that we had run each of the individual simulations long enough for the dynamics of the complex not to be affected by the starting crystal structure conformation, we compared the global dynamics of the VCBC complex over sequential 100-ns blocks of simulation time using σ-r plots (34) (Fig. S2). The similarity of the global motions based on σ-r plots, as well as the magnitude of the first five eigenvalues from PCA (Fig. S1) show that the VCBC dynamics had equilibrated after 300 ns and the VCBC-CUL5ntd dynamics after 100 ns. We collected 300 ns of simulation time after this equilibration period from eight independent simulations to compare the VCBC and VCBC-CUL5ntd ensembles. Not all of the eight independent simulations of VCBC sampled the entire space of PC values (Fig. S2), which indicates that the data from one independent simulation are correlated and sampling is not complete, even after 300 ns of simulation time. Therefore, we treated each independent simulation as one data point when comparing the VCBC ensemble to the VCBC-CUL5 ensemble in Table 1. Although each simulation sampled a limited space in PC1 and PC2, both the mean PC2 values and the PC1 and PC2 variance (range of motion) within an individual simulation were significantly different in the VCBC simulations compared to the VCBC-Cul5 simulations.

To investigate local conformational changes associated with the global dynamics of the VCBC complex observed by PCA, we measured protein backbone conformational changes and hydrogen-bonding patterns. Overall, there were no major conformational changes within each of the protein domains, and most secondary structure elements were maintained to a similar degree in the VCBC and VCBC-CUL5ntd simulations (Fig. S4). The regions with the largest differences in backbone fluctuations were in highly flexible loops or termini (Fig. 3). In particular, the ELOC loop (residues 45–62) is restricted by direct interactions with CUL5 in the VCBC-CU5ntd simulations, and the

TABLE 1 Comparison of Average PC Value for Each Construct Simulated

	PC1		PC2	
	Mean (Å)	Average SD (Å)	Mean (Å)	Average SD (Å)
VCBC-CUL5ntd	−22	20	−32	32
VCBC	24	53[a]	−263[b]	75[a]
VCBC-A3Fctd	−19	25	−89	54[a]
VCBC truncated	54	44	−143[b]	99[a]

[a]p-value < 0.001 relative to the VCBC-CUL5ntd ensemble.
[b]p-value < 0.01 relative to the VCBC-CUL5ntd ensemble

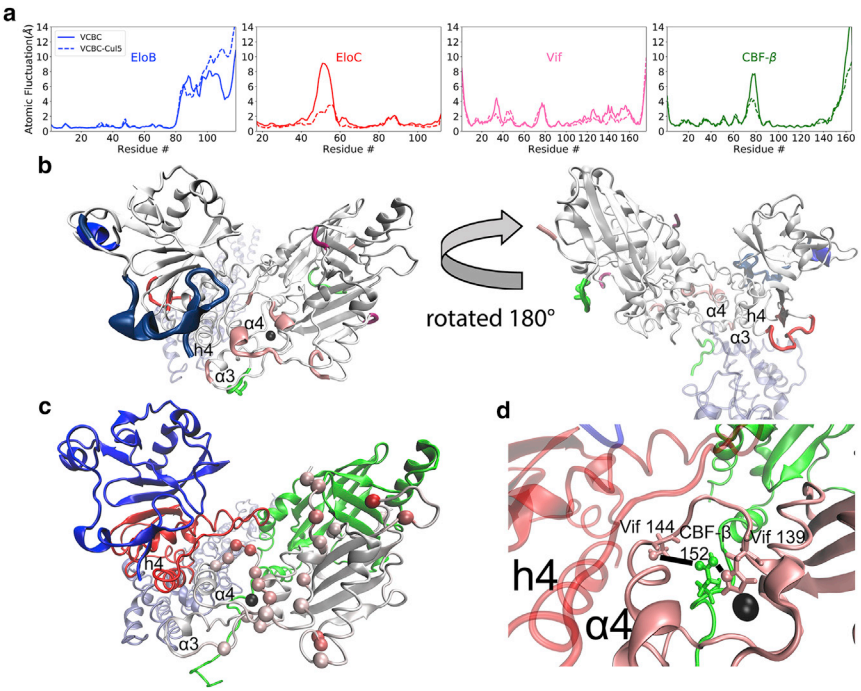

FIGURE 3 (*a*) Root mean-square fluctuations of the individual protein backbones for each protein in the VCBC complex by residue. Each protein is aligned separately before the fluctuations are calculated, so these fluctuations reflect local motions only. The dashed line represents the VCBC-CUL5ntd simulations and the solid line represents the VCBC simulations. (*b*) The VCBC-CUL5ntd structure is shown from two perspectives with the differences from (*a*) highlighted on the structure. CUL5ntd is shown in metallic light blue and VCBC in white, with the regions that undergo more backbone fluctuations in the VCBC simulations than in the VCBC-CUL5ntd simulations (by at least 1 Å root mean-square fluctuation) shown with increased thickness and in color: pink is for Vif, green for CBF-β, blue for ELOB, and red is for ELOC. Regions that undergo more backbone fluctuations for VCBC-CUL5ntd are shown in dark blue for EloB and dark pink for Vif. Vif helices α3 and α4 and ELOC helix h4 are labeled. (*c*) VCBC structure with Vif backbone colored by the difference in average dihedral angle in the VCBC simulations compared to the VCBC-CUL5ntd simulations is shown. Red indicates residues that sample different ϕ or ψ dihedral angles in the VCBC simulations compared to the VCBC-CUL5ntd simulations, whereas white residues have similar average dihedral angles in both sets of simulations. The largest Vif backbone dihedral difference is 149°. Residues that showed an average dihedral angle difference of more than 20° between the VCBC-CUL5ntd simulations and VCBC simulations are shown as spheres. CBF-β is green, ELOB is blue, ELOC is red, and the zinc ion is black. (*d*) A close-up of side chains involved in linker hydrogen bonds with CBF-β Glu152 is shown. Black lines indicate where the hydrogen bonds form. To see this figure in color, go online.

EloB C-terminal region (residues 99–118) is highly flexible in all simulations. Fig. 3 highlights the residues of the Vif sequence with root mean-square backbone fluctuations more than 1 Å greater in the VCBC simulations than in the VCBC-CUL5ntd simulations. These residues are in the linker region and a loop in the α/β-domain that directly interacts with the linker region (Fig. 3 *b*). Additionally, α-helices adjacent to the linker were slightly destabilized in the VCBC simulations without CUL5ntd (Fig. S3). Rearrangement of this linker region is likely necessary for the global conformational changes that reorient the other proteins relative to each other, and this results in greater flexibility in this region when there are global conformational changes.

Examining the Vif backbone dihedral angles sampled, we observed that several residues can sample multiple backbone conformations, and we compared the average Vif backbone dihedral angles in the VCBC and VCBC-CUL5 ensembles. We found that most of the Vif residues where the backbone conformation changes in the two ensembles were in the linker region (Fig. 3 *c*), but not directly at the CUL5 interface. A comparison of hydrogen-bonding patterns also points toward the Vif linker region. We compared all of the hydrogen bonds present in the complex and identified which residues show a difference in hydrogen-bonding pattern in the VCBC simulations compared to the VCBC-CUL5ntd simulations (Fig. S6). The only hydrogen bonds that showed a large difference between the two ensembles are shown in Fig. 3 *d* and are in the Vif linker region. These residues, His139 (part of the HCCH zinc-binding motif) and Ser144, hydrogen bond with Glu152 on the CBF-β C-terminal tail much more often in the VCBC-CUL5ntd simulations than in the simulations with only VCBC, although they do not interact directly with CUL5.

To better characterize the conformational changes in the VCBC ensemble, we divided it into three clusters based on PC1 and PC2 (Fig. 4 *a*). Cluster 1 is most similar to the crystal structure, and almost all of the VCBC-CUL5ntd ensemble falls into this cluster (Fig. 4 *b*). Cluster 2 captures VCBC structures that are slightly more closed in the clamshell (PC2) mode but also twisted to the right (PC1) compared to the crystal structure. Cluster 3 is twisted much more to the left (PC1) than the crystal structure, whereas ELOB and CBF-β are on average even closer together (PC2). Table 2 summarizes the structural differences between the clusters. Clusters 2 and 3 both have a lower occupancy of the two CBF-β Glu152 hydrogen bonds as well as more flexible Vif linkers, which sample backbone dihedral angles that differ from the VCBC-CUL5ntd ensemble. Because large-scale motions involve small concerted changes in multiple dihedral angles, we cannot specify particular backbone dihedral angles that correspond to PC1 and PC2 conformational changes; however, overall local structural changes in the Vif linker region coincide

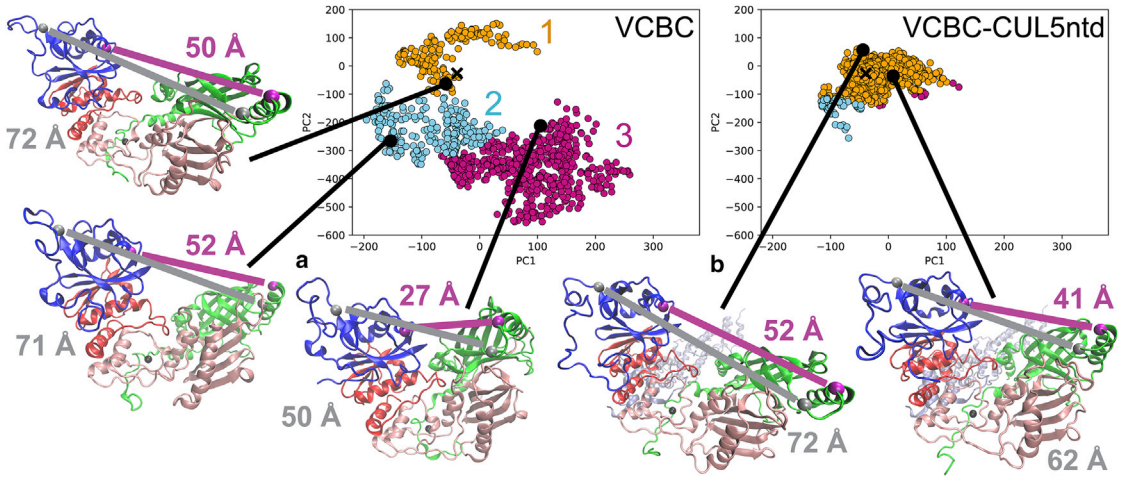

FIGURE 4 Alternate conformations of the Vif protein complex.

Figure360▷ For a Figure360 author presentation of this figure, see https://doi.org/10.1016/j.bpj.2019.03.014.

(*a*) Projection of the VCBC ensemble onto the first two PCs of motion (Å). Clustering was performed based on PC1 and PC2, and the color represents the membership in three different clusters. (*b*) Projection of the VCBC-CUL5ntd ensemble onto the first two PCs of motion (Å). The color of the data points indicates which of the three clusters from the VCBC clustering (plot *a*) the VCBC-CUL5ntd data is classified into. The black x in plots (*a*) and (*b*) represents the values of PC1 and PC2 in the crystal structure from which all simulations were initiated. Example snapshots from the VCBC and VCBC-CUL5 ensembles are shown. Vif is shown in pink, CBF-β in green, ELOB in blue, ELOC in red, the zinc ion in black, and CUL5ntd in metallic light blue. Distances that are most correlated with PC1 and PC2 are indicated for each snapshot. The distance between ELOB 80 and CBF-β 33 is shown in gray (PC1), and the distance between ELOB 58 and CBF-β 37 is shown in magenta (PC2). To see this figure in color, go online.

with the large-scale conformational changes captured by PCA. This suggests that general flexibility in the Vif linker region is necessary for the overall expansion, contraction, and twisting of the VCBC complex that occurs when CUL5 is not bound.

NMR of the VCBC complex

To experimentally observe the conformational heterogeneity of the VCBC complex, we performed methyl-TROSY NMR spectroscopy on ILVMA ^{13}C-labeled VCBC. Because only ILVMA residues are visible, the number of crosspeaks in the two-dimensional spectrum are reduced; therefore, this technique enables observations of methyl resonances in molecular assemblies as large as the proteasome (45). The resonance intensities are sensitive to dephasing that occurs because of conformational changes on the μs-ms timescale, including global conformational changes or self-association, which, in the limit of intermediate exchange, would cause peaks to broaden and disappear (46). The VCBC complex is difficult to work with at the concentrations needed for NMR spectroscopy because of its tendency to aggregate and precipitate at high concentration. To prevent aggregation, the complex can be kept in a buffer with high salt (500 mM NaCl) and 10% glycerol, but the NMR signal is broadened under these conditions and individual methyl peaks are not visible. We found that a defined length of single-stranded DNA (ssDNA) will bind the VCBC complex (Fig. S7) and enable it to be concentrated under low-salt conditions (20 mM NaCl) with no glycerol present, possibly by shielding the positively charged Vif from nonspecific electrostatic interactions with other copies of the complex. Using fluorescence anisotropy measurements, we found that the optimal ssDNA length is 14 oligonucleotides (dT14), binding to VCBC with low nanomolar affinity, $K_d = 3.7 \pm 1.7$ nM (Fig. 5, *a* and *b*). We also noticed that VCBC forms a dimer when DNA is present, as observed by SEC in line with multiangle laser light scattering (Fig. 5 *c*). Because many CRL complexes are known to form dimers, and the dimerization is often mediated by the substrate-binding or adaptor proteins, this dimer of the

TABLE 2 Structural Comparison of VCBC Clusters

	VCBC-CUL5ntd	VCBC	Cluster 1	Cluster 2	Cluster 3
ELOB 80–CBF-β 33 distance (Å) (correlated with PC1)	68 (3)	61 (6)	64 (5)	65 (5)	58 (5)
ELOB 58–CBF-β 37 distance (Å) (correlated with PC2)	46 (3)	39 (7)	42 (5)	45 (6)	36 (5)
Ensemble with at least one Vif–CBF-β 152 H-bond (%)	87	56	92	54	48
Linker dihedral SD (°)	24	32	23	29	30
Linker dihedral RMSD[a] (°)	0	44	38	52	43
No. linker dihedral angles different[a]	0	15	8	20	22

For distances, SDs are noted in parentheses.

[a]Compared to the average linker dihedral angles in the VCBC-CUL5ntd ensemble.

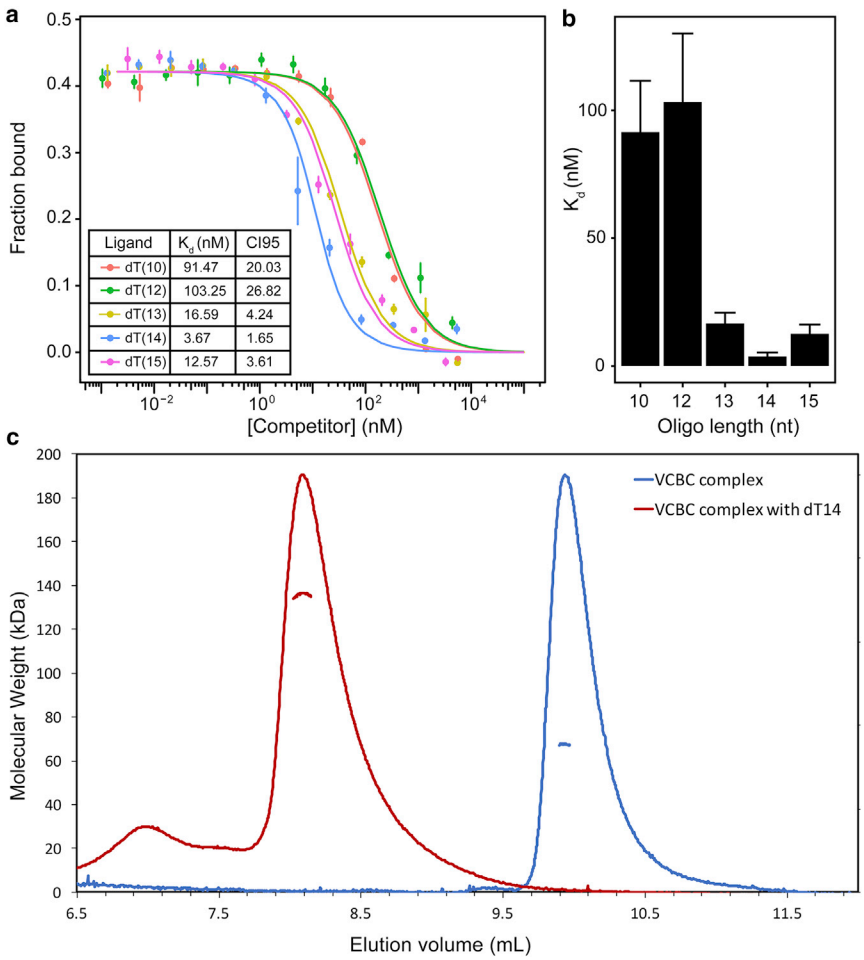

FIGURE 5 Characterization of VCBC interactions with DNA. (*a*) Fluorescence anisotropy data for VCBC-oligonucleotide interactions under competitive binding conditions are shown. Points are the means of three independent experiments, and error bars indicate the SD. (*b*) K_d values determined for the fitted curves shown in (*a*) are shown. Error bars indicate CI95. (*c*) SEC with multiangle laser light scattering of the VCBC complex in the absence (*blue*) and presence (*red*) of dT14 is shown. The elution volume of the VCBC complex in 300 mM NaCl (*blue*) corresponds to an experimental molecular mass of 67 kDa, which is consistent with the theoretical molecular weight for a monomer of 66 kDa. The elution volume of VCBC complex bound to dT14 in 50 mM NaCl (*red*) corresponds to an experimental molecular mass of 135 kDa, which is consistent with the theoretical molecular weight for a dimer of 132 kDa. To see this figure in color, go online.

Vif complex may be the functionally relevant species (47–54). There is no structure available of the VCBC dimer and the residues involved in the dimerization interface have not been investigated. Therefore, we could not perform MD on the VCBC dimer to determine how dimerization might affect the VCBC dynamics seen in our simulations.

We collected methyl-TROSY NMR of the ^{13}C-ILVMA-labeled VCBC complex bound to dT14 (Fig. 6). The resulting VCBC-dT14 spectrum contains few observable methyl peaks. For example, out of 28 Ile residues in the VCBC complex, only 2 or 3 peaks in the Ile-C_δ region of the spectrum were resolved. The absence of expected methyl peaks indicates that dynamics on the μs-ms timescale are causing peak broadening due to motions occurring on the NMR chemical shift timescale (i.e., the intermediate exchange regime). Although the timescale is longer than the nanosecond dynamics observed in our simulations, the broadening of most methyl peaks is consistent with the large-scale conformational rearrangements from MD. Table S3 gives the number of methyl groups that are present in the complex, of which only a small number are visible. The difference in the timescale of dynamics compared to our MD data may be due to the effects of dimerization because our MD simulations were performed on the VCBC monomer. Although dimerization might be expected to restrict conformational sampling, the methyl-TROSY data show that the VCBC complex undergoes conformational exchange even as a dimer.

Effect of A3Fctd on the dynamics of the VCBC complex

NMR of VCBC-A3Fctd

To further test predictions of the MD simulations, we hoped to collect NMR data of the VCBC complex with an additional protein partner bound to observe any change in the conformational exchange visible in the methyl-TROSY data. We attempted these experiments with CUL5ntd bound as in our simulations; however, these NMR experiments were not tractable and could not yield resolved spectra even with deuterated VCBC proteins. Although we were not able to collect NMR data on the VCBC-CUL5ntd complex, other proteins that bind the VCBC complex could be

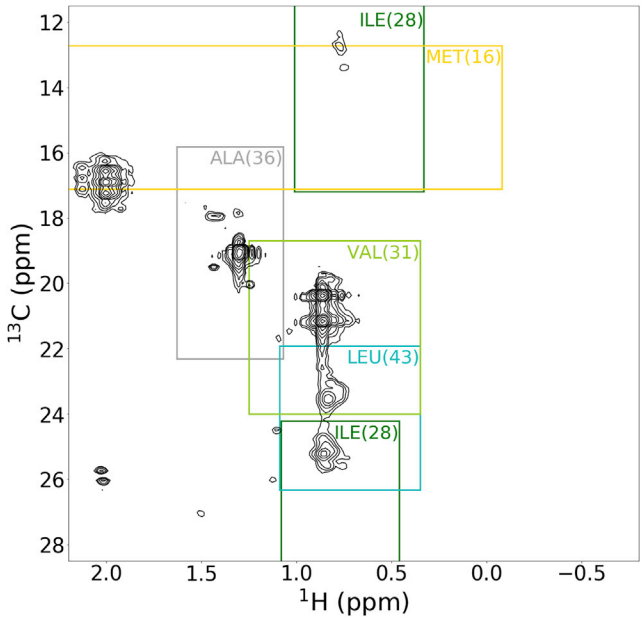

FIGURE 6 ^{13}C-^{1}H methyl-TROSY spectrum of the VCBC complex with ^{13}C isotope labels on Ile, Leu, Val, Met, and Ala (ILVMA) residues recorded at 800 MHz at 300 K. 14-T ssDNA is present to stabilize the VCBC complex. The lowest contour level plotted is 0.4×10^6. Boxes indicate the typical range where the methyl peaks from each residue type are found (57). The number in parentheses indicates the number of peaks we would expect to see in that region given the sequences of the proteins present in the VCBC complex. To see this figure in color, go online.

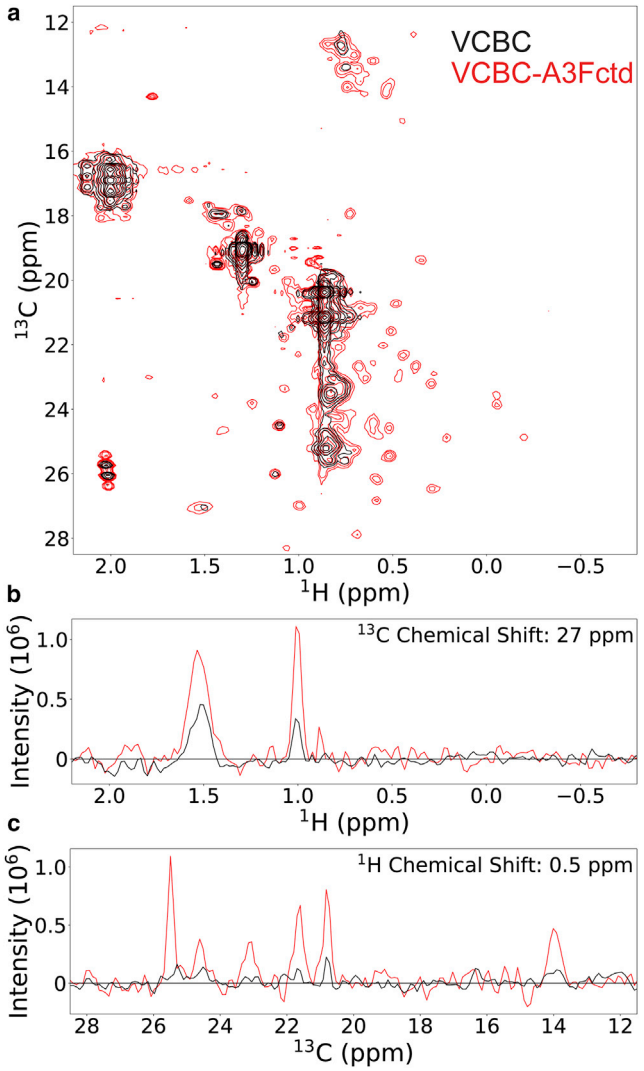

FIGURE 7 ^{13}C-^{1}H methyl-TROSY spectrum of the VCBC complex with and without A3Fctd. (*a*) ^{13}C-^{1}H methyl-TROSY spectrum of the VCBC complex bound to the A3Fctd (*red*) with the spectrum of the VCBC complex (*black*) is shown. The VCBC complex proteins have ^{13}C isotope labels on Ile, Leu, Val, Met, Ala (ILVMA) residues, whereas the A3Fctd is unlabeled. Both spectra have 14-T ssDNA present to stabilize the VCBC complex and are recorded at 800 MHz at 300 K. The lowest contour level plotted for both spectra is 0.4×10^6. (*b*) A one-dimensional cross section of the spectrum at ^{13}C chemical shift of 27 ppm showing two of the methyl peaks is shown. (*c*) A one-dimensional cross section of the spectrum at ^{1}H chemical shift of 0.5 ppm showing six of the methyl peaks is shown. To see this figure in color, go online.

hypothesized to have similar effects on the overall dynamics of the complex; therefore, we decided to investigate the VCBC complex bound to a substrate protein, specifically A3F. Before performing NMR experiments, we wanted to ensure that the presence of DNA would not influence the way that A3F interacts with the VCBC complex. Isothermal titration calorimetry (ITC) experiments showed that A3Fctd, which is the domain that binds to Vif (17), binds to VCBC (in high salt) and VCBC-dT14 (in low salt) with nearly identical affinities (Fig. S9). ITC experiments show that the dimerization of the VCBC-dT14 complex does not affect VCBC affinity for A3Fctd, and additional SEC experiments show that VCBC-dT14 remains a dimer even after A3Fctd binds (Fig. S10).

The VCBC-dT14-A3Fctd construct had better spectroscopic behavior than VCBC-dT14-CUL5ntd, and we were able to resolve a methyl-TROSY spectrum of VCBC from this construct (Fig. 7, *red spectrum*). This spectrum contained many more visible methyl-TROSY peaks than the VCBC spectrum without A3Fctd bound (Fig. 7; Table S3). In total, we observed at least 50 distinct additional methyl resonances for VCBC with A3Fctd bound compared to without A3Fctd. Although not all of the methyl groups in the VCBC complex were resolved for the VCBC-A3Fctd, substantially more peaks were present, indicating that binding of A3Fctd reduces the conformational exchange on the intermediate timescale for several ILVMA residues in the complex, resulting in less broadening of those resonances. For example, out of 28 Ile residues in the VCBC complex, we see ~15 peaks in the Ile-C_δ region of the spectrum for the VCBC-A3Fctd, rather than only two or three peaks for the VCBC complex without A3Fctd. A3Fctd binding must be the cause of the reduction in dynamics because both experiments were performed on VCBC with dT14 present. As in our simulations with and without CUL5ntd bound, this

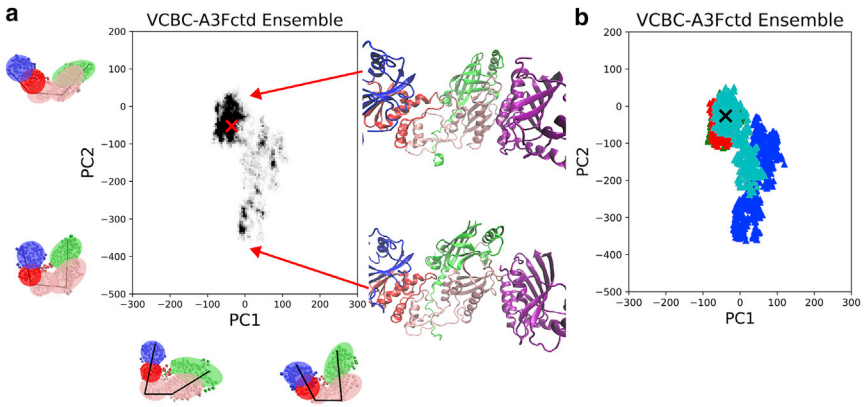

FIGURE 8 Projection of the VCBC-A3Fctd ensembles onto the first two PCs of motion (Å). In (*a*), the shading of the cell represents the fraction of the ensemble at that value of PC1 and PC2, where black is 5.4×10^{-5} or greater and white is 0. In (*b*), each independent simulation is shown in a different color. The x represents the values of PC1 and PC2 in the crystal structure from which all simulations were initiated. Two example snapshots of VCBC-A3Fctd from the simulations are shown. Vif is shown in pink, CBF-β in green, ELOB in blue, ELOC in red, the zinc ion in black, and A3Fctd in purple. To see this figure in color, go online.

indicates that the VCBC complex is dynamic and occupies alternate conformational states, which are restricted when another protein partner binds to the complex and alters the conformational energy landscape.

MD simulations of the VCBC-A3Fctd

Based on our simulations of VCBC-CUL5ntd and the Methyl-TROSY data of the VCBC-A3Fctd, we suspected that A3Fctd might have a similar effect to CUL5ntd, restricting the global motions of the VCBC complex. There is no solved experimental structure of A3Fctd bound to Vif that could be used to initiate MD simulations of the VCBC-A3Fctd complex, but Richards et al. (17) have published a modeled structure of the Vif-A3F interface based on mutational data. We used this model to initiate MD simulations of the VCBC-A3Fctd complex. After running four independent simulations of the VCBC-A3Fctd complex for 400 ns, we projected the conformations sampled in the last 300 ns of each simulation onto the coordinates of correlated motion that were identified based on PCA of the VCBC and VCBC-CUL5ntd simulations to determine if the complex exhibited similar motions when bound to A3Fctd (Fig. 8). The mean and SDs for PC1 and PC2 are given in Table 1. Although the VCBC-A3Fctd samples a wider range of values than the VCBC-CUL5ntd complex along PC2, it does not sample as many alternate conformations as the VCBC complex and generally adopts a conformation that is closer to the VCBC-CUL5ntd crystal structure. Consistent with our NMR data (Fig. 7), the comparison of VCBC and VCBC-A3Fctd in terms of these global conformational changes indicates that the binding of A3Fctd reduces the dynamics of the VCBC complex.

The VCBC-A3Fctd simulations were not as consistent as the VCBC or VCBC-CUL5ntd simulations. As shown in Fig. 8, two of the four VCBC-A3Fctd simulations sampled states close to the crystal structure (similarly to VCBC-CUL5ntd), whereas two simulations sampled more widely along PC2, indicating a clamshell opening of the complex. The VCBC-A3Fctd trajectories that changed conformation may have resulted from an initial unstable A3F-Vif interface because this construct was initiated based on a computational model and not on an experimentally determined structure. The two simulations that diverged the most from the crystal structure along PC1 and PC2 also showed some separation of the A3Fctd protein from the rest of the VCBC complex (Fig. 8). Therefore, the increased dynamics of VCBC in these simulations may occur because A3Fctd begins to unbind from the rest of the complex because of a high-energy initial structure.

DISCUSSION

All-atom simulations of the VCBC complex predict that this complex is conformationally heterogenous, exhibiting large twisting and clamshell motions and a flexible hinge in the Vif linker region near the zinc coordination site. By contrast, the crystal structure of the VCBC-CUL5ntd complex shows a well-defined and compact tertiary structure (4). However, several types of experimental data support increased conformational heterogeneity of the VCBC complex as observed in our MD simulations. Our NMR studies support the model that VCBC undergoes global conformational changes on the μs-ms timescale, and that binding of the A3Fctd protein to the complex reduces these motions allosterically. Binding of other proteins, such as CUL5 and other A3s may also reduce dynamics.

Although MD simulations show that CUL5ntd quenches the dynamics of the VCBC complex, we were unable to observe this quenching by NMR as we did for VCBC-A3Fntd. There are several possible explanations for the broadening of the VCBC-CUL5ntd spectrum, including partial unfolding of the truncated CUL5ntd construct or increased tumbling time of the larger dimeric complex. Alternatively, the VCBC-CUL5ntd complex might exhibit motions on a timescale that we cannot sample in the MD simulations. It is difficult to distinguish between these different possibilities experimentally; however, the dynamics that were sampled in our MD simulations indicate that the VCBC complex is much more conformationally diverse without CUL5 bound.

Previously reported small-angle x-ray scattering data also indicate that the VCBC complex may be more flexible alone than when bound to CUL5 (6). The envelope calculated by

small-angle x-ray scattering was more elongated than the VCBC complex bound to CUL5ntd in the crystal structure, indicating that the VCBC complex alone can sample more extended conformations (6). A recent electron microscopy (EM) study of VCBC bound to antibody antigen-binding fragments (Fabs) also indicates flexibility in the VCBC complex, likely caused by the hinge at the linker region between the two Vif domains (19). The magnitude of conformational heterogeneity of VCBC we observe by MD and NMR would likely make EM of the VCBC complex alone intractable, but the binding of the Fabs stabilizes the complex enough that Binning et al. (19) were able to classify the VCBC-Fab particles into two structurally similar EM maps. Overall, data from experiments and our simulations indicate that although the HIV-1 Vif protein can fold and form a stable complex with only ELOB, ELOC, and CBF-β, additional binding partners further restrict the conformational landscape of Vif.

Previous MD simulations on a human CRL complex by Liu and Nussinov (12,13) revealed conformational changes within the linker between the two domains of the substrate-binding protein that correlated with changes in distance between the E2 ligase and substrate, which are critical for ubiquitin transfer. Similarly, in our VCBC simulations, the large-scale reorientation of the subunits that we observe could assist in the accurate positioning of A3 proteins for ubiquitination. Notably, although VCBC exhibits larger conformational changes in our simulations, the VCBC-CUL5ntd complex also undergoes the same type of global motions involving rotation around the hinge in the Vif linker, but to a smaller degree. These conformational changes may therefore take place within the Vif CRL holoenzyme complex during the ubiquitination process.

Conformational flexibility of the VCBC complex may also be relevant for its ability to ubiquitinate multiple A3 proteins, some of which, like A3F and A3G, bind the ubiquitination complex at different sites on Vif (10,11,15,16). Although it is possible that all A3 proteins could rigidify the VCBC complex to the same extent and in the same conformation, other intrinsically disordered proteins have been demonstrated to adopt different conformations with their multiple binding partners (55,56). Recent work by Binning et al. (19) also showed that Vif disrupts the A3 protein packaging into virions by a degradation-independent mechanism that occurs when CUL5 is prevented from binding to the VCBC complex. The mechanism by which Vif prevents A3 protein packaging could potentially involve alternate conformations of the VCBC complex as observed in our MD simulations. Much remains to be learned about how Vif functions in human cells, and the conformational heterogeneity that it exhibits in complex with human proteins could be important for enabling its multiple functions.

Finally, alternate conformations of the VCBC complex, whether or not they are functionally relevant, may provide a strategy for therapeutically targeting Vif. A small molecule that could trap Vif in a nonfunctional conformation (e.g., by binding selectively to certain conformations of the linker region) could prevent A3 protein ubiquitination and degradation or potentially prevent A3 proteins from binding VCBC at all. Future studies of the conformational ensemble of VCBC with mutations in the Vif linker region would help to test the hypothesis that changes to the local interactions in this region could restrict the VCBC conformational ensemble and could set the stage for therapeutic developments. The computational and NMR results presented here support the model that Vif retains flexibility when bound to the human CRL complex proteins, conferring conformational flexibility on the larger complex, which may have implications for Vif function and potential therapeutic intervention.

SUPPORTING MATERIAL

Supporting Material can be found online at https://doi.org/10.1016/j.bpj.2019.03.014.

AUTHOR CONTRIBUTIONS

K.A.B. proposed the project. K.A.B., J.D.G., J.M.B., and M.P.J. designed the research approach. K.A.B., L.M.C., E.T., and S.T. performed the simulations and analyzed the data. K.A.B., D.J.S., H.M.T., and L.B. performed the experiments and analyzed the data. K.A.B., L.M.C., J.M.B., M.P.J., and J.D.G. wrote the article. K.A.B., L.M.C., D.J.S., E.T., S.T., H.M.T., L.B., J.M.B., M.P.J., and J.D.G. edited the article.

ACKNOWLEDGMENTS

We thank Hiroshi Matsuo, National Cancer Institute, for the kind gift of A3Fctd with 11 mutations plasmid and Elena Conti of the Max Planck Institute of Biochemistry for the gift of the budding yeast Upf1 expression plasmid.

This work was supported by National Institutes of Health grant P50 GM082250 to M.P.J. and J.D.G., F32 GM114894 to K.A.B., and F32 AI120867 to J.M.B. Support was provided by Skidmore College to K.A.B. and by the Skidmore Faculty Student Summer Research Program to L.M.C. and E.T.

REFERENCES

1. Hultquist, J. F., J. A. Lengyel, …, R. S. Harris. 2011. Human and rhesus APOBEC3D, APOBEC3F, APOBEC3G, and APOBEC3H demonstrate a conserved capacity to restrict Vif-deficient HIV-1. *J. Virol.* 85:11220–11234.
2. Harris, R. S., J. F. Hultquist, and D. T. Evans. 2012. The restriction factors of human immunodeficiency virus. *J. Biol. Chem.* 287:40875–40883.
3. Gifford, R. J. 2012. Viral evolution in deep time: lentiviruses and mammals. *Trends Genet.* 28:89–100.
4. Guo, Y., L. Dong, …, Z. Huang. 2014. Structural basis for hijacking CBF-β and CUL5 E3 ligase complex by HIV-1 Vif. *Nature.* 505:229–233.
5. Jäger, S., P. Cimermancic, …, N. J. Krogan. 2011. Global landscape of HIV-human protein complexes. *Nature.* 481:365–370.

6. Kim, D. Y., E. Kwon, …, J. D. Gross. 2013. CBFβ stabilizes HIV Vif to counteract APOBEC3 at the expense of RUNX1 target gene expression. *Mol. Cell.* 49:632–644.
7. Reingewertz, T. H., D. E. Shalev, and A. Friedler. 2010. Structural disorder in the HIV-1 Vif protein and interaction-dependent gain of structure. *Protein Pept. Lett.* 17:988–998.
8. Guo, J., and H. X. Zhou. 2016. Protein allostery and conformational dynamics. *Chem. Rev.* 116:6503–6515.
9. Pierce, N. W., J. E. Lee, …, R. J. Deshaies. 2013. Cand1 promotes assembly of new SCF complexes through dynamic exchange of F box proteins. *Cell.* 153:206–215.
10. Desimmie, B. A., K. A. Delviks-Frankenberrry, …, V. K. Pathak. 2014. Multiple APOBEC3 restriction factors for HIV-1 and one Vif to rule them all. *J. Mol. Biol.* 426:1220–1245.
11. Salter, J. D., G. A. Morales, and H. C. Smith. 2014. Structural insights for HIV-1 therapeutic strategies targeting Vif. *Trends Biochem. Sci.* 39:373–380.
12. Liu, J., and R. Nussinov. 2009. The mechanism of ubiquitination in the cullin-RING E3 ligase machinery: conformational control of substrate orientation. *PLoS Comput. Biol.* 5:e1000527.
13. Liu, J., and R. Nussinov. 2010. Molecular dynamics reveal the essential role of linker motions in the function of cullin-RING E3 ligases. *J. Mol. Biol.* 396:1508–1523.
14. Liu, J., and R. Nussinov. 2010. Rbx1 flexible linker facilitates cullin-RING ligase function before neddylation and after deneddylation. *Biophys. J.* 99:736–744.
15. Russell, R. A., and V. K. Pathak. 2007. Identification of two distinct human immunodeficiency virus type 1 Vif determinants critical for interactions with human APOBEC3G and APOBEC3F. *J. Virol.* 81:8201–8210.
16. Yamashita, T., K. Kamada, …, M. Nomaguchi. 2008. Identification of amino acid residues in HIV-1 Vif critical for binding and exclusion of APOBEC3G/F. *Microbes Infect.* 10:1142–1149.
17. Richards, C., J. S. Albin, …, R. S. Harris. 2015. The binding interface between human APOBEC3F and HIV-1 Vif elucidated by genetic and computational approaches. *Cell Rep.* 13:1781–1788.
18. Soto, C. S., M. Fasnacht, …, B. Honig. 2008. Loop modeling: sampling, filtering, and scoring. *Proteins.* 70:834–843.
19. Binning, J. M., A. M. Smith, …, J. D. Gross. 2018. Fab-based inhibitors reveal ubiquitin independent functions for HIV Vif neutralization of APOBEC3 restriction factors. *PLoS Pathog.* 14:e1006830.
20. Jacobson, M. P., R. A. Friesner, …, B. Honig. 2002. On the role of the crystal environment in determining protein side-chain conformations. *J. Mol. Biol.* 320:597–608.
21. Jacobson, M. P., D. L. Pincus, …, R. A. Friesner. 2004. A hierarchical approach to all-atom protein loop prediction. *Proteins.* 55:351–367.
22. Schrödinger 2014. Maestro, version 9.9. Schrödinger, LLC, New York, NY).
23. Lu, Z., J. R. C. Bergeron, …, M. R. Sanderson. 2013. Insight into the HIV-1 Vif SOCS-box-ElonginBC interaction. *Open Biol.* 3:130100.
24. Humphrey, W., A. Dalke, and K. Schulten. 1996. VMD: visual molecular dynamics. *J. Mol. Graph.* 14:33–38, 27–28.
25. Stone, J. E.; University of Missouri. 1998. An Efficient Library for Parallel Ray Tracing and Animation. University of Missouri, Rolla, MO.
26. Case, D. A., R. M. Betz, …, P. A. Kollman. 2016. Amber 16. University of California, San Francisco.
27. Hornak, V., R. Abel, …, C. Simmerling. 2006. Comparison of multiple Amber force fields and development of improved protein backbone parameters. *Proteins.* 65:712–725.
28. Jorgensen, W. L., J. Chandrasekhar, …, M. L. Klein. 1983. Comparison of simple potential functions for simulating liquid water. *J. Chem. Phys.* 79:926–935.
29. Pang, Y. P., K. Xu, …, F. G. Prendergas. 2000. Successful molecular dynamics simulation of the zinc-bound farnesyltransferase using the cationic dummy atom approach. *Protein Sci.* 9:1857–1865.
30. Andrea, T. A., W. C. Swope, and H. C. Andersen. 1983. The role of long ranged forces in determining the structure and properties of liquid water. *J. Chem. Phys.* 79:4576–4584.
31. Andersen, H. C. 1980. Molecular dynamics simulations at constant pressure and/or temperature. *J. Chem. Phys.* 72:2384–2393.
32. Berendsen, H. J. C., J. P. M. Postma, …, J. R. Haak. 1984. Molecular dynamics with coupling to an external bath. *J. Chem. Phys.* 81:3684–3690.
33. Pedregosa, F., G. Varoquaux, …, É. Duchesnay. 2011. Scikit-learn: machine learning in Python. *J. Mach. Learn. Res.* 12:2825–2830.
34. Zhou, H., S. Li, and L. Makowski. 2016. Visualizing global properties of a molecular dynamics trajectory. *Proteins.* 84:82–91.
35. Stone, M. J., W. Ruf, …, P. E. Wright. 1995. Recombinant soluble human tissue factor secreted by Saccharomyces cerevisiae and refolded from Escherichia coli inclusion bodies: glycosylation of mutants, activity and physical characterization. *Biochem. J.* 310:605–614.
36. Bohn, M. F., S. M. Shandilya, …, C. A. Schiffer. 2013. Crystal structure of the DNA cytosine deaminase APOBEC3F: the catalytically active and HIV-1 Vif-binding domain. *Structure.* 21:1042–1050.
37. Chakrabarti, S., U. Jayachandran, …, E. Conti. 2011. Molecular mechanisms for the RNA-dependent ATPase activity of Upf1 and its regulation by Upf2. *Mol. Cell.* 41:693–703.
38. Schneider, C. A., W. S. Rasband, and K. W. Eliceiri. 2012. NIH Image to ImageJ: 25 years of image analysis. *Nat. Methods.* 9:671–675.
39. Elzhov, T. V., K. M. Mullen, …, B. Bolker. 2016. minpack. Lm: R interface to the Levenberg-Marquardt nonlinear least-squares algorithm found in MINPACK, plus support for bounds. R Foundation for Statistical Computing.
40. Roehrl, M. H., J. Y. Wang, and G. Wagner. 2004. A general framework for development and data analysis of competitive high-throughput screens for small-molecule inhibitors of protein-protein interactions by fluorescence polarization. *Biochemistry.* 43:16056–16066.
41. Wickham, H. 2016. ggplot2. Cham. Springer International Publishing, New York.
42. Tugarinov, V., P. M. Hwang, …, L. E. Kay. 2003. Cross-correlated relaxation enhanced 1H[bond]13C NMR spectroscopy of methyl groups in very high molecular weight proteins and protein complexes. *J. Am. Chem. Soc.* 125:10420–10428.
43. Delaglio, F., S. Grzesiek, …, A. Bax. 1995. NMRPipe: a multidimensional spectral processing system based on UNIX pipes. *J. Biomol. NMR.* 6:277–293.
44. Helmus, J. J., and C. P. Jaroniec. 2013. Nmrglue: an open source Python package for the analysis of multidimensional NMR data. *J. Biomol. NMR.* 55:355–367.
45. Sprangers, R., and L. E. Kay. 2007. Quantitative dynamics and binding studies of the 20S proteasome by NMR. *Nature.* 445:618–622.
46. Mittermaier, A., and L. E. Kay. 2006. New tools provide new insights in NMR studies of protein dynamics. *Science.* 312:224–228.
47. Ahn, J., Z. Novince, …, A. M. Gronenborn. 2011. The Cullin-RING E3 ubiquitin ligase CRL4-DCAF1 complex dimerizes via a short helical region in DCAF1. *Biochemistry.* 50:1359–1367.
48. Chew, E. H., T. Poobalasingam, …, T. Hagen. 2007. Characterization of cullin-based E3 ubiquitin ligases in intact mammalian cells–evidence for cullin dimerization. *Cell. Signal.* 19:1071–1080.
49. Choo, Y. Y., and T. Hagen. 2012. Mechanism of cullin3 E3 ubiquitin ligase dimerization. *PLoS One.* 7:e41350.
50. McMahon, M., N. Thomas, …, J. D. Hayes. 2006. Dimerization of substrate adaptors can facilitate cullin-mediated ubiquitylation of proteins by a "tethering" mechanism: a two-site interaction model for the Nrf2-Keap1 complex. *J. Biol. Chem.* 281:24756–24768.
51. Merlet, J., J. Burger, …, L. Pintard. 2009. Regulation of cullin-RING E3 ubiquitin-ligases by neddylation and dimerization. *Cell. Mol. Life Sci.* 66:1924–1938.
52. Okumura, F., A. Joo-Okumura, …, T. Kamura. 2016. The role of cullin 5-containing ubiquitin ligases. *Cell Div.* 11:1.

53. Andresen, C. A., S. Smedegaard, …, A. Flores-Morales. 2014. Protein interaction screening for the ankyrin repeats and suppressor of cytokine signaling (SOCS) box (ASB) family identify Asb11 as a novel endoplasmic reticulum resident ubiquitin ligase. *J. Biol. Chem.* 289:2043–2054.

54. Wu, W., and X. H. Sun. 2011. A mechanism underlying notch-induced and ubiquitin-mediated Jak3 degradation. *J. Biol. Chem.* 286:41153–41162.

55. Dyson, H. J. 2016. Making sense of intrinsically disordered proteins. *Biophys. J.* 110:1013–1016.

56. Wright, P. E., and H. J. Dyson. 2015. Intrinsically disordered proteins in cellular signalling and regulation. *Nat. Rev. Mol. Cell Biol.* 16:18–29.

57. Ulrich, E. L., H. Akutsu, …, J. L. Markley. 2008. BioMagResBank. *Nucleic Acids Res.* 36:D402–D408.